

# Mesoscale ocean fronts enhance carbon export due to gravitational sinking and subduction

Michael R. Stukel<sup>a,1</sup>, Lihini I. Aluwihare<sup>b</sup>, Katherine A. Barbeau<sup>b</sup>, Alexander M. Chekalyuk<sup>c</sup>, Ralf Goericke<sup>b</sup>, Arthur J. Miller<sup>b</sup>, Mark D. Ohman<sup>b</sup>, Angel Ruacho<sup>b</sup>, Hajoon Song<sup>d</sup>, Brandon M. Stephens<sup>b</sup>, and Michael R. Landry<sup>b</sup>

<sup>a</sup>Earth, Ocean, and Atmospheric Science Department, Florida State University, Tallahassee, FL 32306; <sup>b</sup>Scripps Institution of Oceanography, University of California, San Diego, La Jolla, CA 92093; <sup>c</sup>Lamont-Doherty Earth Observatory, Columbia University, Palisades, NY 10964; and <sup>d</sup>Department of Earth, Atmospheric and Planetary Sciences, Massachusetts Institute of Technology, Cambridge, MA 02139

Edited by David M. Karl, University of Hawaii, Honolulu, HI, and approved December 28, 2016 (received for review June 10, 2016)

**Enhanced vertical carbon transport (gravitational sinking and subduction) at mesoscale ocean fronts may explain the demonstrated imbalance of new production and sinking particle export in coastal upwelling ecosystems. Based on flux assessments from  $^{238}\text{U}$ - $^{234}\text{Th}$  disequilibrium and sediment traps, we found 2 to 3 times higher rates of gravitational particle export near a deep-water front ( $305 \text{ mg C m}^{-2} \cdot \text{d}^{-1}$ ) compared with adjacent water or to mean (nonfrontal) regional conditions. Elevated particle flux at the front was mechanically linked to Fe-stressed diatoms and high mesozooplankton fecal pellet production. Using a data assimilative regional ocean model fit to measured conditions, we estimate that an additional  $\sim 225 \text{ mg C m}^{-2} \cdot \text{d}^{-1}$  was exported as subduction of particle-rich water at the front, highlighting a transport mechanism that is not captured by sediment traps and is poorly quantified by most models and in situ measurements. Mesoscale fronts may be responsible for over a quarter of total organic carbon sequestration in the California Current and other coastal upwelling ecosystems.**

particle flux | particulate organic carbon | plankton | carbon cycle | biological carbon pump

The magnitude of plankton-mediated primary production (PP) that is removed annually from the surface ocean–atmosphere system and transported to depth remains poorly constrained, with estimates varying from  $5 \text{ Pg C yr}^{-1}$  to  $21 \text{ Pg C yr}^{-1}$  (1–3). Inadequate resolution of the many mechanisms that drive export flux—sinking particles and aggregates, active transport by vertically migrating organisms, advection and diffusion of particles and dissolved organic compounds—is also a major challenge for parameterizing ocean models that seek to predict future responses to climate impacts. Although sinking material is generally assumed to dominate the export of organic carbon in the oceans, sinking flux is often significantly lower than simultaneously measured new or net community production (4–6) and insufficient to meet the metabolic requirements of deep-sea and benthic organisms (7). This has led to the notion of mesoscale ocean features (fronts and eddies) as sites where locally enhanced vertical advection may stimulate production and gravitational (sinking) export (8–10), or move bulk suspended organic matter to depth during subduction events (11–13). Due to the complex 3D structure and temporal variability of these features, however, simultaneous quantification of sinking and subduction has not been achieved previously in any observational field study.

The southern California Current Ecosystem (CCE) is a productive eastern boundary current biome representative of coastal upwelling ecosystems worldwide. Nearshore waters off of Point Conception are typically cold, salty, and nutrient-rich due to upwelling, whereas the southward-flowing California Current forms a low-salinity band that separates the coastal upwelling region from oligotrophic subtropical waters further offshore. Although the coastal CCE has high primary productivity (14) and nitrate uptake (15–17), the vertical export of carbon as sinking particles (assessed by both sediment traps and  $^{238}\text{U}$ - $^{234}\text{Th}$  disequilibrium) is comparatively low (18, 19). Both models and in situ data suggest that this production–export imbalance results, in part, from lateral

transport of particles produced in the coastal area to the offshore region where net export is expected (20–23). However, the expected high export ratio in offshore waters of the CCE is not supported by existing in situ measurements (19, 24).

Submesoscale and mesoscale fronts are common features in the southern CCE and are increasing in frequency (25). These features are often locations with enhanced nutrient input to the surface layer and elevated biological standing stocks and particle concentrations (26–28). To understand the potential roles of frontal systems in carbon export via both gravitational sinking and subduction, we studied a frontal region inshore of the California Current off Southern California in August 2012 using a combination of transect sampling and Lagrangian experiments (i.e., tracking the temporal evolution of water parcels). In the results presented in *Results and Discussion*, we (i) quantify phytoplankton carbon production; (ii) determine vertical carbon transport due to sinking particles using sediment trap and  $^{234}\text{Th}$  methods; (iii) evaluate potential mechanisms driving enhanced gravitational flux, including mesozooplankton fecal pellet production and diatom trace metal limitation; and (iv) estimate subduction of particles to depth using a data assimilative Regional Ocean Modeling System (ROMS) model.

## Results and Discussion

We found that gravitational flux was amplified approximately twofold at the front relative to surrounding waters or typical non-frontal regions of the CCE, and that subduction of organic matter contributed additional export of comparable magnitude. The former finding is based on high  $^{238}\text{U}$ - $^{234}\text{Th}$  deficiency and large particle fluxes into sediment traps in the frontal region. The latter

### Significance

**Transport of organic carbon from the sunlit surface ocean to deeper depths drives net oceanic uptake of  $\text{CO}_2$  from the atmosphere. However, mechanisms that control this carbon export remain poorly constrained, limiting our ability to model and predict future changes in this globally important process. We show that the flux of sinking particles (typically considered the dominant form of downward transport of organic carbon) is twice as high at a frontal system, relative to surrounding waters or to nonfrontal conditions. Furthermore, downward transport by subduction leads to additional carbon export at the front that is similar in magnitude to the sinking flux. Such enhanced C export at episodic and mesoscale features needs to be incorporated into biogeochemical forecast models.**

Author contributions: M.R.S., L.I.A., K.A.B., A.M.C., R.G., A.J.M., M.D.O., and M.R.L. designed research; M.R.S., K.A.B., R.G., M.D.O., A.R., H.S., B.M.S., and M.R.L. performed research; M.R.S., L.I.A., K.A.B., A.M.C., R.G., A.J.M., M.D.O., A.R., H.S., and B.M.S. analyzed data; and M.R.S. wrote the paper.

The authors declare no conflict of interest.

This article is a PNAS Direct Submission.

<sup>1</sup>To whom correspondence should be addressed. Email: mstukel@fsu.edu.

This article contains supporting information online at [www.pnas.org/lookup/suppl/doi:10.1073/pnas.1609435114/-DCSupplemental](http://www.pnas.org/lookup/suppl/doi:10.1073/pnas.1609435114/-DCSupplemental).

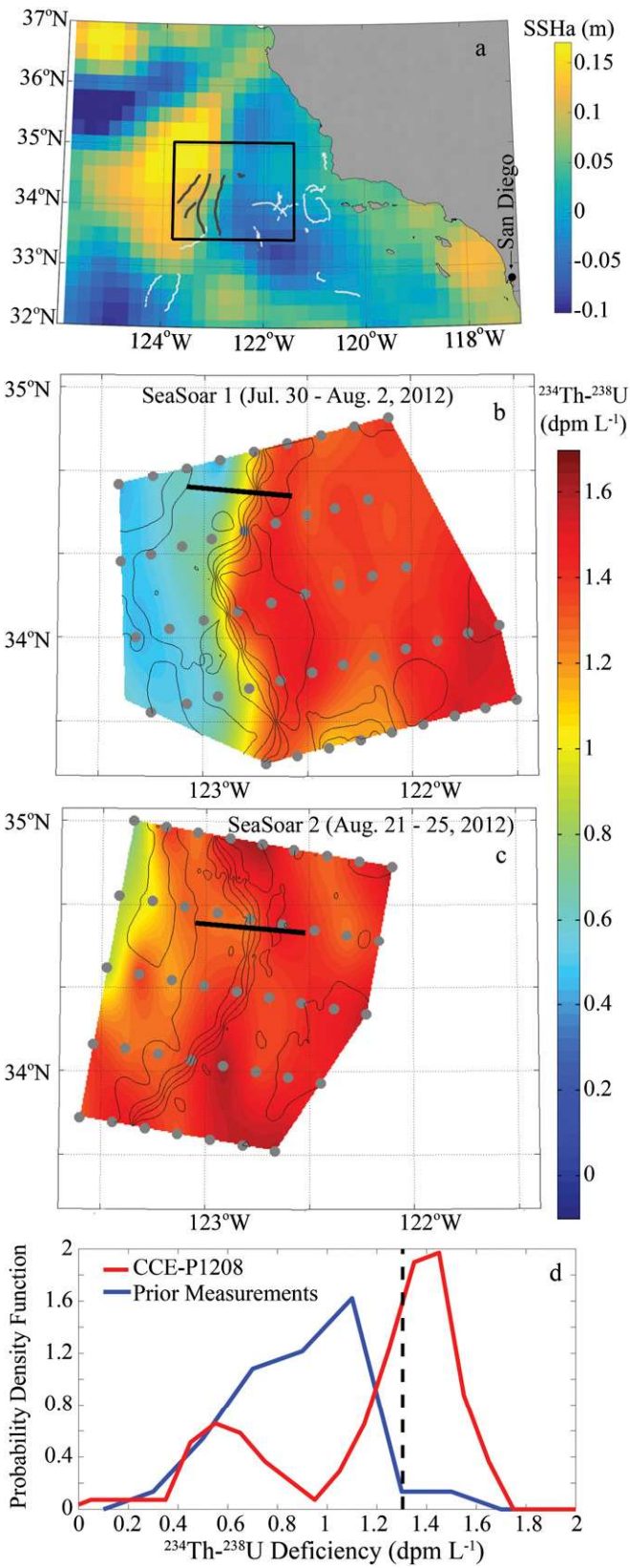


**Fig. 1.** (A) Study region in the CCE with satellite-tracked drifter trajectories (black tracks within rectangle) and Archiving, Validation and Interpretation of Satellite Oceanographic data (AVISO) sea-surface height anomalies (SSHa) on 9 August (cruise midpoint). Thin white tracks are locations of Lagrangian cycles on previous CCE LTER cruises (19, 22). (B and C) The  $^{238}\text{U}$ - $^{234}\text{Th}$  deficiency measured in surface seawater on (B) SeaSoar Survey 1 and (C) SeaSoar Survey 2. (D) Probability density function of surface layer  $^{234}\text{Th}$  deficiency (from SeaSoar surveys). Dashed line is median value on CCE-P1208. High deficiency is indicative of prior gravitational flux.

finding is supported by vertical sections of  $^{234}\text{Th}$ , particulate organic carbon (POC), and total organic carbon (TOC) across the front as well as a physical model assimilating the results of satellite remote sensing products and numerous temperature and salinity profiles in the frontal region. In *Gravitational Flux and Subduction of Organic Matter*, we explain this evidence in detail.

**Gravitational Flux.** The study site was a stable eddy-related frontal region (hereafter E-Front; Fig. 1) characterized by sloping isopycnals (density surfaces), with the  $1,024.5 \text{ kg m}^{-3}$  to  $1,024.9 \text{ kg m}^{-3}$  isopycnal surfaces outcropping near the core of the front and descending to a depth of  $\sim 50$  m on the western (offshore) side of the front (Fig. 2). The strongest surface expression of E-Front was an east–west salinity gradient, with salinity of 33.35 at the front center (Fig. S1). For further analyses, we define the eastern boundary (coastal side) of E-Front as the location where the 33.5-salinity isopleth outcrops to the surface, and the western boundary (offshore) as the location where the  $1,024.2 \text{ kg m}^{-3}$  isopycnal shoals to a depth of 30 m.

Surface sampling during an initial mesoscale survey (30 July to 5 August) showed high  $^{234}\text{Th}$  deficiency (relative to secular equilibrium with  $^{238}\text{U}$ ) on the coastal side of the front, indicating high particle export (Fig. 1B). The E-Front core acted as a barrier separating this high-deficiency water from offshore low-deficiency waters. Three weeks later, a repeat survey showed high surface  $^{234}\text{Th}$  deficiency throughout the study region (Fig. 1C). Including both surveys, surface  $^{234}\text{Th}$  concentrations were lower than typically found in nonfrontal regions of the CCE (Fig. 1D,  $P < 0.01$ , two-sided Mann–Whitney  $u$  test), indicating high  $^{234}\text{Th}$  deficiency and enhanced particle export. In fact, the median deficiency was higher than all but one previous surface measurement of  $^{234}\text{Th}$  made in nonfrontal regions on three previous month-long cruises in the CCE. This finding suggests that export near the front was substantially higher than would be expected in the region when fronts are absent. Although enhanced vertical flux at the front is not conclusively demonstrated by the  $^{234}\text{Th}$  results alone due to the long half-life of  $^{234}\text{Th}$  ( $\sim 24$  d) relative to the short residence time of water in the front (3 to 4 d, based on drifter trajectories), this conclusion is also supported by the sinking material collected in shallow drifting sediment traps.

We deployed sediment traps during five Lagrangian experiments (hereafter “cycles”) in the core of and to either side of E-Front. Temperature–salinity (T-S) plots (Fig. S24) showed that cycle 1 sampled the portion of E-Front with outcropping isopycnals, whereas cycles 2 and 5 sampled the western portion of E-Front where front expression was predominantly subsurface (with cycle 5 slightly closer to the center of the front). Cycles 3 and 4 sampled nonfrontal water on the coastal and offshore sides, respectively, of E-Front. Sediment traps showed significantly higher carbon export near the base of the euphotic zone at the front (cycle 1,  $437 \pm 25 \text{ mg C m}^{-2} \cdot \text{d}^{-1}$ ) than measured in the offshore (cycle 4,  $133 \pm 18 \text{ mg C m}^{-2} \cdot \text{d}^{-1}$ ) or coastal (cycle 3,  $150 \pm 32 \text{ mg C m}^{-2} \cdot \text{d}^{-1}$ ) locations. Cycle 1 export was twofold greater than the highest sediment trap flux previously measured in nonfrontal waters of the CCE (Fig. 3A), corroborating the  $^{234}\text{Th}$  inferences of high local export in the frontal region. Enhanced export was also found for cycle 5 ( $328 \pm 24 \text{ mg C m}^{-2} \cdot \text{d}^{-1}$ ), conducted in waters with features most closely resembling the region of subsurface expression of the front, but not for cycle 2 ( $150 \pm 68 \text{ mg C m}^{-2} \cdot \text{d}^{-1}$ ).

We also estimated sinking particle flux from two high-resolution vertical sections across the front (Fig. 2) using a steady-state  $^{238}\text{U}$ - $^{234}\text{Th}$  deficiency equation (Fig. 3B). Although this approach

---

Thick black lines show the locations of front crossings 1 and 2. Thin black lines are sea surface salinity. (D) Probability density function of surface layer  $^{234}\text{Th}$  deficiency (from SeaSoar surveys). Dashed line is median value on CCE-P1208. High deficiency is indicative of prior gravitational flux.

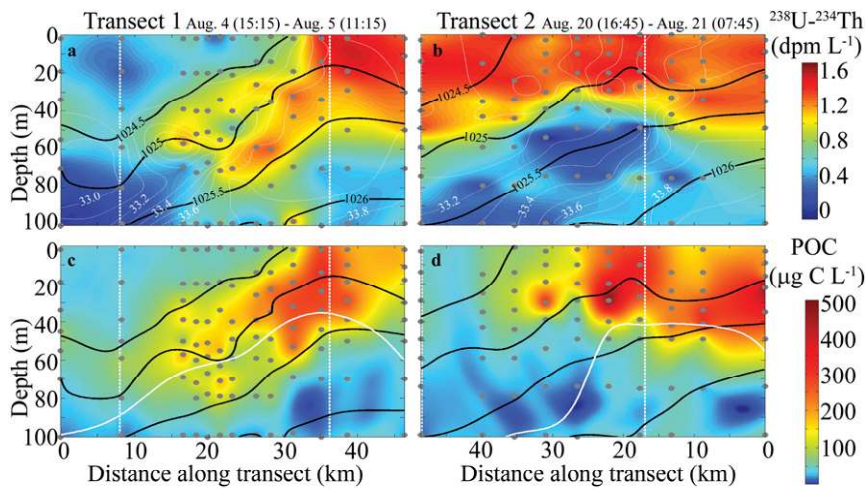


**Fig. 2.** The  $^{238}\text{U}$ - $^{234}\text{Th}$  deficiency measured on vertical sections across the front for (A) section 1 and (B) section 2. Black lines are density contours. Note the subduction feature along the 1,025 isopycnal in A (from 15 to 30 km along transect) and its absence from B. (C and D) Particulate organic carbon concentrations on (C) front crossing 1 and (D) front crossing 2. White lines show depth of the euphotic zone (0.1% light level). Vertical dashed white lines show front boundaries as defined in *Gravitational Flux*.

has substantial uncertainty due to the complex 3D structure of E-Front and the short residence time of water in the feature, this simple export proxy produced results similar to the sediment traps, showing elevated export relative to typical measurements made from  $^{234}\text{Th}$  in the CCE. Averaging the steady-state export estimates for the two transects, 104 mg C·m<sup>-2</sup>·d<sup>-1</sup> (84 to 124, mean and 95% C.I.) for transect 1 and 185 (135 to 232) mg C·m<sup>-2</sup>·d<sup>-1</sup> for transect 2, these  $^{234}\text{Th}$ -based measurements for the 30-km-wide E-Front are approximately twofold higher than the typical export flux determined by  $^{234}\text{Th}$  in the CCE (80 mg C·m<sup>-2</sup>·d<sup>-1</sup>). Similarly, average export from sediment trap deployments in the frontal region (305 mg C·m<sup>-2</sup>·d<sup>-1</sup>; cycles 1, 2, and 5) was  $\sim 2.5 \times$  higher than the typical nonfrontal value of 121 mg C·m<sup>-2</sup>·d<sup>-1</sup>, as well as greater than the trap fluxes on the offshore or coastal sides of the front (133 and 150 mg C·m<sup>-2</sup>·d<sup>-1</sup>, respectively).

**Subduction of Organic Matter.** The two high-resolution vertical sections across the front showed contrasting spatial patterns of  $^{234}\text{Th}$ . Our initial transect (4–5 August) showed a subsurface deficiency maximum (30 m to 70 m depth) at the front (Fig. 2A), which could result from subduction of high-deficiency surface waters or from localized subsurface particle production and sinking. Although the latter scenario is known to occur in offshore oligotrophic regions of the CCE, we found no evidence of subsurface PP maxima in any of our five Lagrangian cycles or in a PP model parameterized from cruise data, which showed most productivity in the upper 25 m of the water column. The measured  $^{234}\text{Th}$  section thus suggests along-isopycnal subduction of high-deficiency water from the coastal side of the front. This along-isopycnal  $^{234}\text{Th}$  feature was further associated with enhanced subsurface concentrations of POC (Fig. 2C) and TOC (Fig. S3), consistent with POC subduction at the front. In contrast, similar measurements 2 wk later did not show evidence of frontal subduction (Fig. 2B) but rather a shoaling of the  $^{234}\text{Th}$  isocline between isopycnals 1,025 and 1,025.5 kg·m<sup>-3</sup> caused by mild upwelling. Such differences are an expected feature of dynamic fronts, in which meanders produce alternating regions of subduction and upwelling. Such dynamics (combined with the long half-life of  $^{234}\text{Th}$ ) also likely explain the larger-scale patterns of surface  $^{234}\text{Th}$  during our transects (Fig. 1). Downwelling conditions lead to convergent frontal features that set stark boundaries between coastal (high deficiency) and offshore (low deficiency) water. Upwelling conditions lead to divergent features, with high gravitational flux at the front creating a wider high-deficiency signature.

To further investigate and quantify the export flux from subduction, we used a dynamically consistent, data-assimilating ROMS model (29, 30). Consistent with observational interpretations, modeled vertical velocities confirmed relatively strong subduction over most of E-Front during transect 1 and weak upwelling during transect 2 (Fig. 4). Using measured POC and  $\Delta\text{TOC}$  (the difference between E-Front TOC and typical deep-water TOC) concentrations at the base of the euphotic zone and modeled vertical velocities, we calculated areally averaged POC subduction rates of 475 (270 to 687, 95% C.I.) and  $-25$  ( $-82$  to  $31$ ) mg C·m<sup>-2</sup>·d<sup>-1</sup> for transects 1 and 2, respectively, and  $\Delta\text{TOC}$  subduction rates of 379 (195 to 549) and  $-17$  ( $-60$  to  $28$ ) mg C·m<sup>-2</sup>·d<sup>-1</sup>. The fate of the subducted POC is unknown, but it coincided with high subsurface  $\text{NH}_4^+$  concentrations ( $>1 \mu\text{mol L}^{-1}$ ) on transect 1, suggesting rapid remineralization beneath the euphotic zone. Importantly, this advective transport, averaging 225 (POC) or 181 ( $\Delta\text{TOC}$ ) mg C·m<sup>-2</sup>·d<sup>-1</sup>, must be added to the gravitational flux (305 mg C·m<sup>-2</sup>·d<sup>-1</sup>) to determine total export enhancement at E-Front, because the subducted bulk suspended material is not measured by sediment traps or  $^{234}\text{Th}$ : $^{238}\text{U}$  deficiency.

Using a chlorophyll-light diagnostic model parameterized with measured  $^{14}\text{C}$  PP from the Lagrangian cycles, we calculated PP across the transects to determine the fraction of PP exported as POC out of the base of the euphotic zone. Because typical formulations of the  $e$  ratio (export/PP) do not account for advective flux, we define the  $e_{\text{POC}}$  ratio as the sum of advective and sinking POC export divided by  $^{14}\text{C}$  PP. The calculated  $e_{\text{POC}}$  ratio of 67% for transect 1 exceeded the average  $f$  ratio at the front (52%) determined using  $\text{NO}_3^-$  and  $\text{NH}_4^+$  concentrations and an ecosystem model parameterized for the CCE. For transect 2, the  $e_{\text{POC}}$  ratio of 11% was lower than the  $f$  ratio (45%).

**Mechanisms of Enhanced Gravitational Flux.** To elucidate the mechanisms causing enhanced gravitational export at the front, we investigated phytoplankton and zooplankton dynamics during each Lagrangian experiment. Cycle 1 (at the front) had higher vertically integrated  $^{14}\text{C}$  PP ( $1,451 \pm 140$  mg C m<sup>-2</sup>·d<sup>-1</sup>) than coastal or offshore cycles (Fig. 3A). Previous nonfrontal experiments exhibited decreased export efficiency ( $e$  ratio) when PP was high (19, 24). In contrast, at the front (cycle 1), the plankton community maintained a high  $e$  ratio (30%) despite enhanced phytoplankton production.

We evaluated two nonexclusive mechanisms that could cause an increase in export efficiency at the front: mesozooplankton fecal pellet production and increased silicification by diatoms.

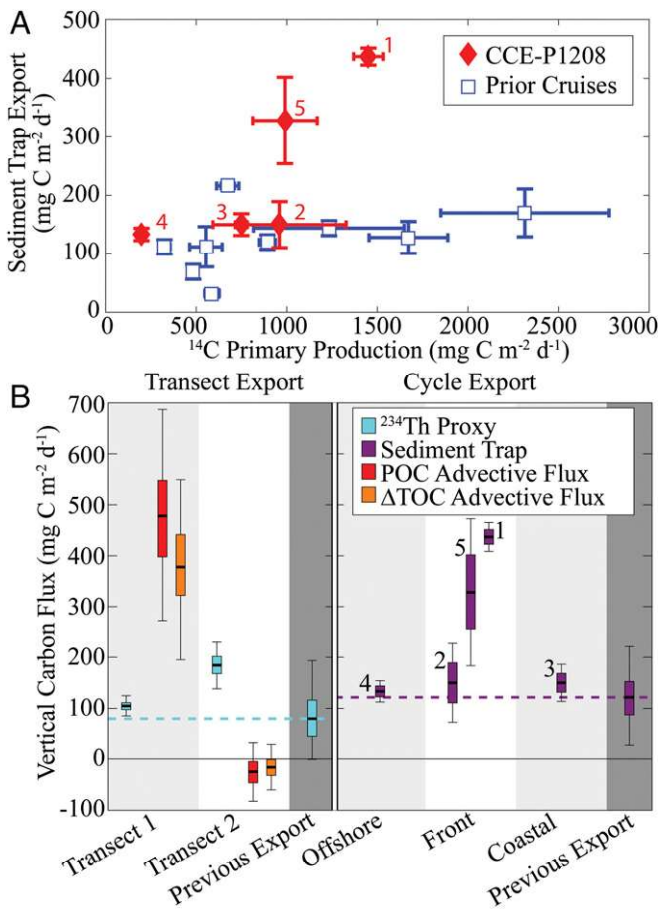


**Fig. 3.** (A) Comparison of CCE-P1208 sediment trap-based export measurements (red) with prior sediment trap measurements made in nonfrontal regions on CCE LTER cruises (blue). Note high export for frontal cycles 1 and 5. (B) Vertical carbon flux at E-Front during transects (*Left*) and Lagrangian cycles (*Right*). Gravitational POC flux was estimated using two approaches:  $^{238}\text{U}$ - $^{234}\text{Th}$  deficiency with a simple steady-state equation without upwelling (blue, *Left*) and sediment traps (purple, *Right*). Advective carbon flux is an additional form of carbon export estimated from vertical velocities and POC (red) or  $\Delta\text{TOC}$  concentrations (orange;  $\Delta\text{TOC}$  is the difference between TOC measured on the transect and deepwater TOC). Boxes show quartiles, and whiskers show 95% confidence intervals. Far right shaded column in both plots indicates previous gravitational POC flux ranges in the CCE region at nonfrontal locations. Horizontal dashed lines show average previous gravitational flux in the CCE determined by sediment trap (purple) and  $^{234}\text{Th}$  (blue). In *Right*, results from nonfrontal cycles 4 and 3 (offshore/left and coastal/right, respectively) are shown for comparison.

Mesozooplankton fecal pellets are major contributors to sinking flux in the CCE (19). Cycle 1 showed substantially enhanced grazing (and mesozooplankton biomass) relative to the other cycles, with grazing rate estimates ( $6.3 \pm 2.9 \text{ mg Chl } a \text{ m}^{-2} \cdot \text{d}^{-1}$ ) on the high side of previous measurements in the CCE (Fig. S2D). Similarly, mesozooplankton herbivory was enhanced at E-Front in transect samples (Fig. 5 E and F), and we measured high concentrations of phaeopigments and high phaeopigment:Chl *a* ratios ( $> 4$ , highest for cycles 1 and 5) in the sediment traps, indicative of high fecal pellet flux produced by herbivorous zooplankton.

Fe limitation has been shown to drive enhanced export in the CCE by increasing silification by diatoms that continue to take up Si despite reduced organic matter production (31). The increased cellular Si:N ratios amplify the ballasting effect of diatoms, leading to higher sinking rates of aggregates and fecal pellets that contain diatoms. Decoupled Si and N uptake also leads to low dissolved  $\text{Si(OH)}_4:\text{NO}_3^-$  ratios in the water column. Negative values of Si

excess [ $\text{Si}_{\text{ex}} = [\text{Si(OH)}_4] - [\text{NO}_3^-] \times R_{\text{Si}:\text{NO}_3}$ , where  $R_{\text{Si}:\text{NO}_3}$  is the  $\text{Si(OH)}_4:\text{NO}_3^-$  ratio of upwelled water, equal to 1 mol:mol for the CCE (32)] are diagnostic of Fe limitation in the CCE and are evident in samples from the E-Front transects (Fig. 5 A and B) and cycle 1 (Fig. S2B). Conversely,  $\text{Si}_{\text{ex}}$  values were high (and grazing low) for cycle 2, the only near-front cycle that did not show enhanced export. Variable fluorescence (indicative of the photosynthetic status of phytoplankton and correlated with Fe availability) was low at the front (Fig. 5 C and D), consistent with Fe limitation. The ratio of nitrate:dissolved Fe (micromolars of  $\text{NO}_3^-$ :nanomolars of dFe) is another diagnostic feature of Fe limitation in the CCE, with ratios in excess of 5 indicating significant potential for Fe limitation of diatoms (31–33). Consistent with our interpretation of Fe limitation in the main axis of the front, we found  $\text{NO}_3^-:\text{dFe}$  values of 10 to 26 in the upper 50 m during cycle 1 and consistently  $>5$  on the coastal edge of the E-Front transects. A 3-d deckboard Fe-enrichment experiment during cycle 1 also showed increased  $\text{NO}_3^-$  drawdown,  $^{15}\text{NO}_3^-$  uptake, and biomass production in Fe-amended bottles relative to control incubations (Fig. S2C). Thus, increased efficiency of carbon export at E-Front appears to be linked to Fe limitation of diatoms, which leads to increased silicification and rapid sinking of the heavily ballasted fecal pellets produced by zooplankton grazing, although other mechanisms may contribute as well.

**Export at Fronts.** Although our study focused on a single mesoscale feature, the two mechanisms that drove high gravitational flux at E-Front are likely common for eastern boundary upwelling systems (EBUS), where fronts are typically associated with elevated phytoplankton and zooplankton biomass (26, 34). For example, Fe limitation was shown to increase export in a gradient region between cyclonic and anticyclonic eddies close to Point Conception (31), and significantly elevated mesozooplankton biomass and organic aggregate abundance (28) were demonstrated at a front ~300 km southeast of E-Front.

Front frequency in the CCE, measured by autonomous in situ gliders along California Cooperative Oceanic Fisheries Investigations (CalCOFI) lines 80 (near our study site) and 90 (extending offshore from the Southern California Bight), indicates that 8% of CCE water is within 15 km of a density front (34). If we assume that the greater than twofold enhancement of gravitational flux at E-Front is generally representative of the region, then over 14% of the total sinking particle flux in the region occurs near mesoscale fronts. Additionally, our mean estimate of  $\sim 225 \text{ mg C m}^{-2} \cdot \text{d}^{-1}$  for advective POC export in subducted water parcels at E-Front suggests that total particle export at CCE fronts may exceed 25% of regional gravitational flux. Given the global importance of EBUS in total oceanic production and the similarity in their physical dynamics at a front ~300 km southeast of E-Front.

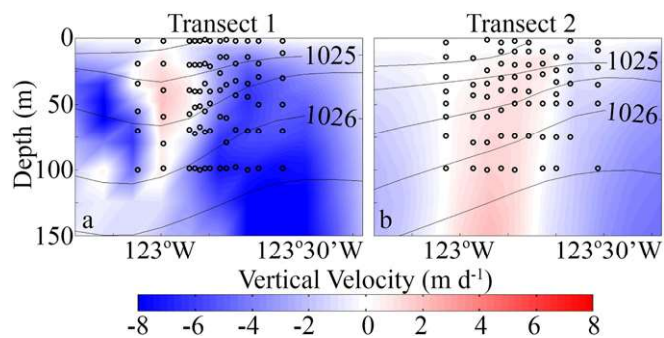


**Fig. 4.** Vertical velocity sections at  $34^{\circ}36'\text{N}$  from the data assimilating ROMS model. Each section is a 6-d average centered at the midpoint sampling time of cross-frontal (A) transect 1 or (B) transect 2. Black lines are isopycnals. Black circles are  $^{234}\text{Th}$  sampling locations. Red shades are positive (upward) velocities, and blue shades are negative (downward) velocities. Note the strongly downward velocities along the core of the front in A and the weak upwelling velocities in B.

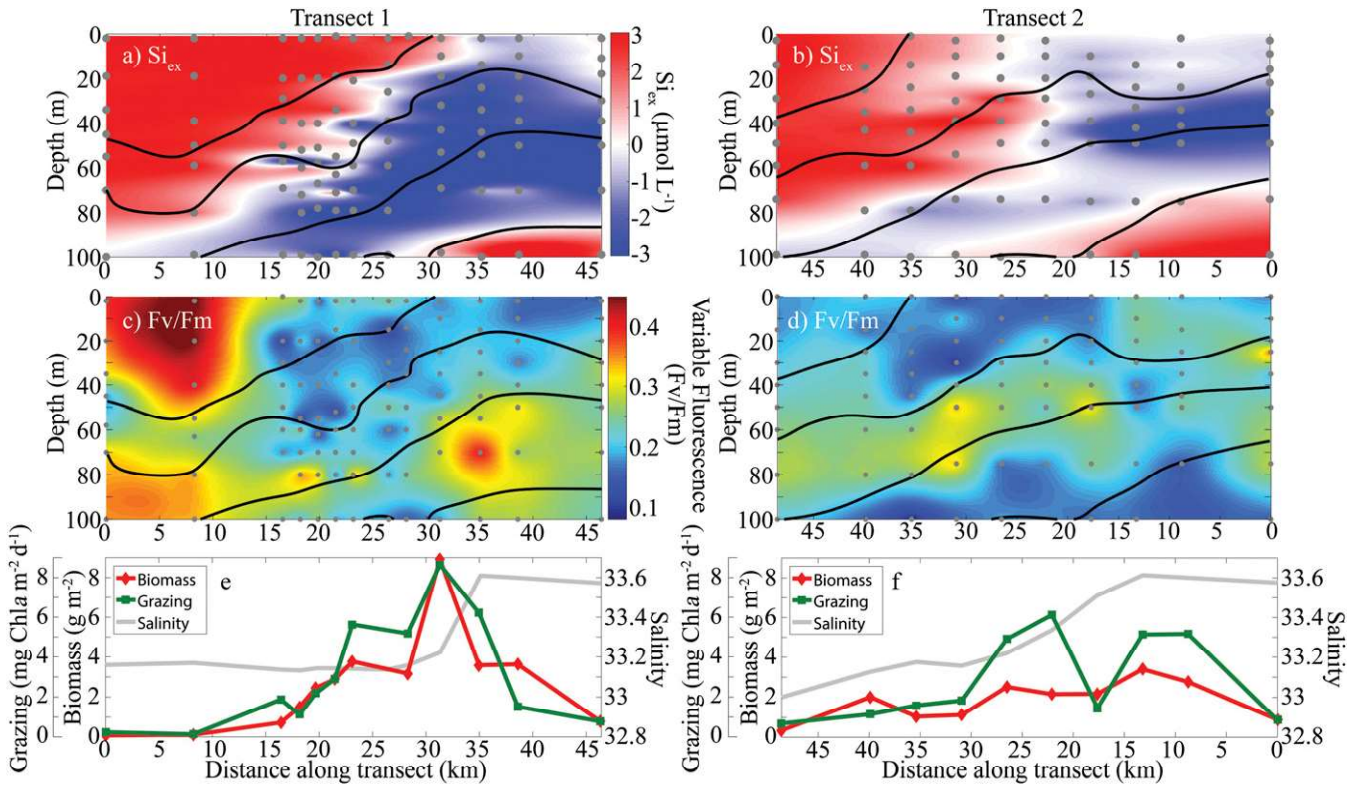


**Fig. 5.** Biological and chemical sections during (A, C, and E) transect 1 and (B, D, and F) transect 2. (A and B)  $\text{Si}_{\text{ex}}$  ( $= [\text{H}_4\text{SiO}_4] - [\text{NO}_3^-] \times R_{\text{Si}: \text{NO}_3}$ ). Negative values are indicative of Fe stress. (C and D) Variable fluorescence ( $\text{Fv}/\text{Fm}$ ). Low values are indicative of Fe stress. (E and F) Mesozooplankton biomass and grazing rates from vertical net tows. Gray lines show surface salinity (gradient region indicates location of the surface expression of E-front).

(35, 36), we can surmise that EBUS fronts are likely globally important loci for carbon transport into the ocean's interior.

Although the present results clearly indicate the importance of mesoscale fronts to carbon sequestration in a contemporary coastal ocean system, they likely underestimate the role of fronts in a warmer, future climate. Within the CCE, a decadal-scale trend of increasing frontal frequency has been linked to long-term increases of upwelling favorable winds (25, 37). Continued strengthening of land-sea temperature differences, combined with increased stratification in other regions, will likely further increase the importance of particle export at mesoscale fronts to the global carbon cycle.

## Materials and Methods

**Cruise Overview.** Our sampling scheme involved three distinct aspects: (i) 3D mapping of the large-scale physical structure of the front with a towed SeaSoar instrument; these surveys (referred to as SeaSoar surveys) were combined with surface mapping of  $^{234}\text{Th}$  deficiency and other biogeochemical properties in the region; (ii) Nearly synoptic 50-km transects across the frontal feature while measuring biogeochemical and ecological properties at 6 to 8 depths at 10 to 13 stations across the front; and (iii) Lagrangian experiments (referred to as "cycles") during which we followed an *in situ* array drogued at 15 m depth, on which we attached bottles for experimental incubations including  $\text{H}^{14}\text{CO}_3^-$  uptake (38). The array provided a moving frame of reference for a suite of other measurements including mesozooplankton biomass and grazing rates,  $^{234}\text{Th}$ - $^{238}\text{U}$  disequilibrium measurements, nutrients, POM, and biological standing stocks. An identically drogued sediment trap array was deployed simultaneously on each cycle.

The front was initially located using satellite sea surface temperature (SST) and sea surface height (SSH), an autonomous Spray glider, and a free-fall Moving Vessel Profiler (28), then the region was mapped (SeaSoar Survey 1) from 30 July to 2 August. This initial survey was immediately followed by cross-frontal transect 1 (4 August, 1515 hours to 5 August, 1115 hours). After transect 1, we conducted the five cycles in different locations relative to the front. Cycles 1 to 5 lasted from 6 to 9 August, 10 to 12 August, 13 to 15 August, 16 to 18 August, and 18 to 20 August, respectively. After completing these experiments, cross-frontal transect 2 was conducted in waters near the

location of transect 1 from 20 August, 1645 hours to 21 August, 0745 hours. The region was mapped again (SeaSoar Survey 2) from 21 to 25 August.

**Export Measurements.** Particle-interceptor trap (PIT)-style sediment traps (19, 39) with 8 to 12 cylindrical, 70-mm-diameter tubes with baffles on top were deployed at a depth near the base of the euphotic zone as determined from fluorescence profiles (60 m for cycles 1 and 3, 70 m on cycles 2 and 5, and 100 m on cycle 4). Tubes were deployed with a formaldehyde brine for a period of ~2.25 d. After recovery, overlying material was removed by suction, and samples were split for C and N analyses by CHN analyzer,  $\text{C}^{234}\text{Th}$  ratio analysis, and pigment measurements (Chl a and phaeopigments) by the acidification method. The  $^{234}\text{Th}$  concentrations were measured using standard small volume methods (40), including a  $^{230}\text{Th}$  tracer spike, filtration and beta counting at sea on a RISO beta counter, background beta counts >6 mo after the cruise, gravimetric addition of  $^{229}\text{Th}$ , and quantification of the  $^{229:230}\text{Th}$  ratio by inductively coupled plasma (ICP) MS at the Woods Hole Oceanographic Institution Analytical Facility. The  $^{238}\text{U}$ - $^{234}\text{Th}$  deficiency was calculated after estimating  $^{238}\text{U}$  activity from salinity (41), assuming steady state, and vertically integrating.

**Biological and Chemical Measurements.** Samples were collected by Niskin bottle for measurements of biological and chemical standing stocks and rates. Chl a was measured by fluorometer with acidification. POC was measured with a CHN analyzer. TOC was measured on a Shimadzu analyzer. Nutrients [ $\text{NO}_3^-$ ,  $\text{NH}_4^+$ ,  $\text{PO}_4^{3-}$ ,  $\text{Si(OH)}_4$ ] were measured by autoanalyzer. Phytoplankton variable fluorescence was measured using the Advanced Laser Fluorometer (42). PP was measured by uptake of  $\text{H}^{14}\text{CO}_3^-$  in triplicate 250-mL bottles incubated in situ for 24 h. Mesozooplankton were collected by vertical (on front transects) or oblique (during semi-Lagrangian cycles) net tows with a 0.71-m diameter, 202- $\mu\text{m}$  mesh bongo net. Mesozooplankton grazing rates were determined from gut fluorescence measurements using gut turnover times calculated from a temperature-dependent equation (43).

**Physical Model and POC Subduction.** To measure the passive transport of organic carbon by subduction, we first used kriging to compute gridded fields of POC and  $\Delta\text{TOC}$  (where  $\Delta\text{TOC}$  is the difference between measured shallow

TOC and average deep TOC concentrations) along the two transects. We then calculated flux using the equations  $J = [\text{POC}] \times w$  or  $J = [\Delta \text{TOC}] \times w$ , where  $J$  is flux (milligrams C per square meter per day) and  $w$  is the vertical velocity (meters per day) derived from a dynamically consistent data-assimilative model. Data assimilation was conducted within the ROMS with a 9-km grid resolution using a four-dimensional variational approach that repeatedly adjusted initial and boundary conditions to minimize the mismatch between the model and physical measurements (e.g., temperature, salinity) measured on our cruise (30).

1. Boyd PW, Trull TW (2007) Understanding the export of biogenic particles in oceanic waters: Is there consensus? *Prog Oceanogr* 72(4):276–312.
2. Henson SA, et al. (2011) A reduced estimate of the strength of the ocean's biological carbon pump. *Geophys Res Lett* 38(4):L04606.
3. Laws EA, Falkowski PG, Smith WO, Ducklow H, McCarthy JJ (2000) Temperature effects on export production in the open ocean. *Global Biogeochem Cycles* 14(4):1231–1246.
4. Emerson S (2014) Annual net community production and the biological carbon flux in the ocean. *Global Biogeochem Cycles* 28(1):14–28.
5. Quay P (1997) Was a carbon balance measured in the equatorial Pacific during JGOFS? *Deep Sea Res Part II Top Stud Oceanogr* 44(9–10):1765–1781.
6. Stukel MR, et al. (2015) The imbalance of new and export production in the Western Antarctic Peninsula, a potentially "leaky" ecosystem. *Global Biogeochem Cycles* 29(9):1400–1420.
7. Burd AB, et al. (2010) Assessing the apparent imbalance between geochemical and biochemical indicators of meso- and bathypelagic biological activity: What the @#! is wrong with present calculations of carbon budgets? *Deep Sea Res Part II Top Stud Oceanogr* 57(16):1557–1571.
8. Benitez-Nelson CR, et al. (2007) Mesoscale eddies drive increased silica export in the subtropical Pacific Ocean. *Science* 316(5827):1017–1021.
9. Maiti K, Benitez-Nelson CR, Lomas MW, Krause JW (2009) Biogeochemical responses to late-winter storms in the Sargasso Sea, III—Estimates of export production using  $^{234}\text{Th}$ : $^{238}\text{U}$  disequilibrium and sediment traps. *Deep Sea Res Part I Oceanogr Res Pap* 56(6):875–891.
10. Fischer G, et al. (2016) Bathypelagic particle flux signatures from a suboxic eddy in the oligotrophic tropical North Atlantic: production, sedimentation and preservation. *Biogeosciences* 13(11):3203–3223.
11. Kadko DC, Washburn L, Jones B (1991) Evidence of subduction within cold filaments of the northern California coastal transition zone. *J Geophys Res Oceans* 96(C8):14909–14926.
12. Omand MM, et al. (2015) Eddy-driven subduction exports particulate organic carbon from the spring bloom. *Science* 348(6231):222–225.
13. Washburn L, et al. (1991) Water mass subduction and the transport of phytoplankton in a coastal upwelling system. *J Geophys Res Oceans* 96(C8):14927–14945.
14. Kahru M, Mitchell BG (2002) Influence of the El Niño-La Niña cycle on satellite-derived primary production in the California Current. *Geophys Res Lett* 29(17):1846.
15. Dugdale RC, Davis CO, Wilkerson FP (1997) Assessment of new production at the upwelling center at Point Conception, California, using nitrate estimated from remotely sensed sea surface temperature. *J Geophys Res Oceans* 102(C4):8573–8585.
16. Dugdale RC, Wilkerson FP (1989) New production in the upwelling center at Point Conception, California - Temporal and spatial patterns. *Deep Sea Res* 36(7):985–1007.
17. Eppley RW, Renger EH, Harrison WG (1979) Nitrate and phytoplankton production in southern California coastal waters. *Limnol Oceanogr* 24(3):483–494.
18. Collins LE, et al. (2011) Particle fluxes in San Pedro Basin, California: A four-year record of sedimentation and physical forcing. *Deep Sea Res Part I Oceanogr Res Pap* 58(8):898–914.
19. Stukel MR, Ohman MD, Benitez-Nelson CR, Landry MR (2013) Contributions of mesozooplankton to vertical carbon export in a coastal upwelling system. *Mar Ecol Prog Ser* 491:47–65.
20. Olivieri RA, Chavez FP (2000) A model of plankton dynamics for the coastal upwelling system of Monterey Bay, California. *Deep Sea Res Part II Top Stud Oceanogr* 47(5–6):1077–1106.
21. Plattner GK, Gruber N, Frenzel H, McWilliams JC (2005) Decoupling marine export production from new production. *Geophys Res Lett* 32(11):L11612.
22. Stukel MR, Landry MR, Benitez-Nelson CR, Goericke R (2011) Trophic cycling and carbon export relationships in the California Current Ecosystem. *Limnol Oceanogr* 56(5):1866–1878.
23. Gruber N, et al. (2011) Eddy-induced reduction of biological production in eastern boundary upwelling systems. *Nat Geosci* 4(11):787–792.
24. Stukel MR, et al. (2015) Using Lagrangian-based process studies to test satellite algorithms of vertical carbon flux in the eastern North Pacific Ocean. *J Geophys Res Oceans* 120(11):7208–7222.
25. Kahru M, Di Lorenzo E, Manzano-Sarabia M, Mitchell BG (2012) Spatial and temporal statistics of sea surface temperature and chlorophyll fronts in the California Current. *J Plankton Res* 34(9):749–760.
26. Landry MR, et al. (2012) Pelagic community responses to a deep-water front in the California Current Ecosystem: Overview of the A-Front Study. *J Plankton Res* 34(9):739–748.
27. Li QP, Franks PJS, Ohman MD, Landry MR (2012) Enhanced nitrate fluxes and biological processes at a frontal zone in the southern California current system. *J Plankton Res* 34(9):790–801.
28. Ohman MD, Powell JR, Picheral M, Jensen DW (2012) Mesozooplankton and particulate matter responses to a deep-water frontal system in the southern California Current System. *J Plankton Res* 34(9):815–827.
29. Miller AJ, Song H, Subramanian AC (2015) The physical oceanographic environment during the CCE-LTER Years: Changes in climate and concepts. *Deep Sea Res Part II Top Stud Oceanogr* 112:6–17.
30. Song H, et al. (2012) Application of a data-assimilation model to variability of Pacific sardine spawning and survivor habitats with ENSO in the California Current System. *J Geophys Res Oceans* 117(C3):C03009.
31. Brzezinski MA, et al. (2015) Enhanced silica ballasting from iron stress sustains carbon export in a frontal zone within the California Current. *J Geophys Res Oceans* 120(7):4654–4669.
32. King AL, Barbeau KA (2011) Dissolved iron and macronutrient distributions in the southern California Current System. *J Geophys Res Oceans* 116(C3):C03018.
33. King AL, Barbeau K (2007) Evidence for phytoplankton iron limitation in the southern California Current System. *Mar Ecol Prog Ser* 342:91–103.
34. Powell JR, Ohman MD (2015) Covariability of zooplankton gradients with glider-detected density fronts in the Southern California Current System. *Deep Sea Res Part II Top Stud Oceanogr* 112:79–90.
35. Sydeman WJ, et al. (2014) Climate change. Climate change and wind intensification in coastal upwelling ecosystems. *Science* 345(6192):77–80.
36. Wang YT, Castelao RM, Yuan YP (2015) Seasonal variability of alongshore winds and sea surface temperature fronts in Eastern Boundary Current Systems. *J Geophys Res Oceans* 120(3):2385–2400.
37. Garcia-Reyes M, Largier J (2010) Observations of increased wind-driven coastal upwelling off central California. *J Geophys Res Oceans* 115(C4):C04011.
38. Landry MR, Ohman MD, Goericke R, Stukel MR, Tsyrklevich K (2009) Lagrangian studies of phytoplankton growth and grazing relationships in a coastal upwelling ecosystem off Southern California. *Prog Oceanogr* 83(1–4):208–216.
39. Knauer GA, Martin JH, Bruland KW (1979) Fluxes of particulate carbon, nitrogen, and phosphorus in the upper water column of the Northeast Pacific. *Deep Sea Res* 26(1):97–108.
40. Pike SM, Buesseler KO, Andrews J, Savoye N (2005) Quantification of  $^{234}\text{Th}$  recovery in small volume sea water samples by inductively coupled plasma-mass spectrometry. *J Radioanal Nucl Chem* 263(2):355–360.
41. Owens SA, Buesseler KO, Sims KWW (2011) Re-evaluating the  $^{238}\text{U}$ -salinity relationship in seawater: Implications for the  $^{238}\text{U}$ : $^{234}\text{Th}$  disequilibrium method. *Mar Chem* 127(1–4):31–39.
42. Chekalyuk A, Hafez M (2008) Advanced laser fluorometry of natural aquatic environments. *Limnol Oceanogr Methods* 6(11):591–609.
43. Dam HG, Peterson WT (1988) The effect of temperature on the gut clearance rate-constant of planktonic copepods. *J Exp Mar Biol Ecol* 123(1):1–14.
44. Strickland JD, Parsons TR (1972) *A Practical Handbook of Seawater Analysis* (Fish Res Board Canada, Ottawa, ON, Canada) 2nd Ed.
45. Chekalyuk AM, Landry MR, Goericke R, Taylor AG, Hafez MA (2012) Laser fluorescence analysis of phytoplankton across a frontal zone in the California Current ecosystem. *J Plankton Res* 34(9):761–777.
46. King AL, Buck KN, Barbeau KA (2012) Quasi-Lagrangian drifter studies of iron speciation and cycling off Point Conception, California. *Mar Chem* 128–129:1–12.
47. Kishi MJ, et al. (2007) NEMURO: A lower trophic level model for the North Pacific marine ecosystem. *Ecol Model* 202(1–2):12–25.
48. Li QP, Franks PJS, Landry MR, Goericke R, Taylor AG (2010) Modeling phytoplankton growth rates and chlorophyll to carbon ratios in California coastal and pelagic ecosystems. *J Geophys Res Biogeosci* 115(G4):G04003.
49. Buesseler KO, Bacon MP, Cochran JK, Livingston HD (1992) Carbon and nitrogen export during the JGOFS North Atlantic Bloom Experiment estimated from  $^{234}\text{Th}$ : $^{238}\text{U}$  disequilibria. *Deep Sea Res Part A* 39(7–8):1115–1137.
50. Coale KH, Bruland KW (1985)  $^{234}\text{Th}$ : $^{238}\text{U}$  disequilibria within the California Current. *Limnol Oceanogr* 30(1):22–33.
51. Benitez-Nelson CR, et al. (2001) Testing a new small-volume technique for determining  $^{234}\text{Th}$  in seawater. *J Radioanal Nucl Chem* 248(3):795–799.
52. Savoye N, et al. (2006)  $^{234}\text{Th}$  sorption and export models in the water column: A review. *Mar Chem* 100(3–4):234–249.
53. Chen JH, Edwards RL, Wasserburg GJ (1986)  $^{238}\text{U}$ ,  $^{234}\text{U}$  and  $^{232}\text{Th}$  in seawater. *Earth Planet Sci Lett* 80(3–4):241–251.
54. de Verneil A (2015) Phytoplankton in surface ocean fronts: Resolving biological dynamics and spatial structure. PhD dissertation (Univ Calif, San Diego, La Jolla, CA).
55. Resplandy L, et al. (2012) How does dynamical spatial variability impact  $^{234}\text{Th}$ -derived estimates of organic export? *Deep Sea Res Part I Oceanogr Res Pap* 68:24–45.
56. Isaaks EH, Srivastava R (1989) *An Introduction to Applied Geostatistics* (Oxford Univ Press, Oxford, UK).
57. Krige DG (1951) A statistical approach to some basic mine valuation problems on the Witwatersrand. *J Chem Metall Min Soc Afr* 52(1):119–139.
58. Stein ML (1999) *Interpolation of Spatial Data: Some Theory for Kriging* (Springer, New York).
59. Bednarek N, Ohman MD (2015) Changes in pteropod distributions and shell dissolution across a frontal system in the California Current System. *Mar Ecol Prog Ser* 523:93–103.
60. de Verneil A, Franks PJS (2015) A pseudo-Lagrangian method for remapping ocean biogeochemical tracer data: Calculation of net Chl-a growth rates. *J Geophys Res Oceans* 120(7):4962–4979.
61. Buesseler KO (1991) Do upper-ocean sediment traps provide an accurate record of particle flux? *Nature* 353(6343):420–423.
62. Stukel MR, et al. (2016) The biological pump in the Costa Rica Dome: An open-ocean upwelling system with high new production and low export. *J Plankton Res* 38(2):348–365.

**ACKNOWLEDGMENTS.** We thank Captain Chris Curl, the crew, and resident marine technicians of the R/V *Melville*, whose efforts made this challenging study possible. We also thank Hugh Ducklow for the loan of the RISO beta counter; Mark Hafez, Megan Roadman, and our many collaborators in the CCE Long Term Ecological Research (LTER) program for help at sea; Peter Franks and Alain De Verneil for insightful discussions of the data; and two anonymous reviewers who provided very helpful feedback. Data used in this study are available on the CCE LTER Datazo website. This study was funded by National Science Foundation Grant OCE-1026607 to the CCE LTER site.